Tubes and Sheets in Shear-stratified Turbulence

Marie FARGE[1] & Alexandre AZZALINI[1]
& Alex MAHALOV[2]& Basil NICOLAENKO[2]& Frank TSE[2]
& Giulio PELLEGRINO[3]& Kai SCHNEIDER[3]

[1] *LMD-CNRS, École Normale Supérieure, Paris*
24, rue Lhomond, 75231 Paris Cedex 5, FRANCE
farge@lmd.ens.fr

[2] *Department of Mathematics, Arizona State University,*
Tempe, AZ 85287-1804, USA

[3] *Centre de Mathématiques et d'Informatique, Université de Provence,*
39, rue F. Joliot–Curie, 13453 Marseille Cedex 13, FRANCE

Abstract Coherent vortex extraction using wavelets is applied to a shear-stratified turbulent flow computed by Direct Numerical Simulations (DNS) to model the atmospheric jet stream in the tropopause. The basic state is characterized by a jet centered at the tropopause and stable density stratification profile with increased stratification above the tropopause. Quasi-equilibrium turbulent flow-fields are obtained after long-time integration of the governing equations written in primitive variables using adaptive spectral domain decomposition method.

I use without any compunction
A well-chosen wavelet function;
With theorems nice,
And methods concise,
My results are immune to debunction.
—H.K. Moffatt, 2001

1. Shear-stratified turbulent flows

We will study a generic situation encountered in geophysical turbulence where there is a competition between shear and stable stratification. Stratification produces sheet-like structures ('pancakes') and waves which may inhibit turbulence caused by the shear and therefore reduce the turbulent mixing. Shear tends to destabilize the interfaces and gives rise to Kelvin-Helmholtz instabilities producing vortex tubes and driving strong mixing.

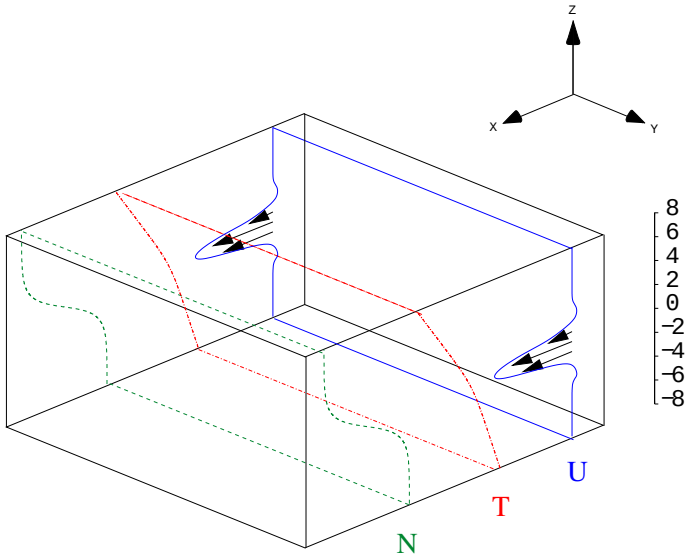

Figure 1. Flow geometry.

We will model jet streams encountered in the Earth atmosphere at the tropopause, which corresponds to the transition between the troposphere and the stratosphere at an altitude about 10 to 15 km depending on the latitude, by considering a jet, with a Gaussian profile for the mean streamwise velocity, in a stably stratified fluid (Fig. 1). The flow consists of a jet core surrounded by two shear layers: the layer above has a positive shear and stronger temperature gradient, while the layer below has a negative shear and presents a weaker temperature gradient, with the buoyancy (Brunt-Väisälä) frequency being reduced by a factor two. The latter configuration is typical of the jet stream at the tropopause.

The Richardson number, which quantifies stratification and is based on the mean velocity gradient, is low (about 2) within the jet core and velocity fluctuations are maximal there, thus producing sustained turbulence. The Richardson number increases towards the jet edges (near $z = \pm 2$) where the effect of stratification tends to reduce turbulence with the shear length-scale exceeding the buoyancy outer scale (Tse, Mahalov, Nicolaenko, & Fernando 2001). The flow in the vicinity of the edges of the jet is locally out of geostrophic equilibrium and thus produces nonlinear gravity waves which travel further away and break (near $z = \pm 4$). These regions far from the jet edges have much weaker velocity fluctuations than in the core, hence turbulent mixing is reduced there, although potential energy and temperature fluctuations remain strong.

This is in agreement with observational studies in Bedard, Canavero & Einaudi 1986. Indeed, critical levels where waves extract energy from the mean flow (near $z = \pm 2$) correspond to those regions of enhanced turbulence, where the Richardson number is below 0.25, hence generating Kelvin-Helmholtz instabilities (Kaltenbach, Gerz & Schumann 1994).

The flow evolution has been computed using 3D Navier–Stokes equations coupled with the heat equation under the Boussinesq approximation. The numerical integration is made using spectral domain decomposition (Tse, Mahalov, Nicolaenko, & Fernando 2001) and considering periodic boundary conditions in the streamwise and spanwise directions, but not in the vertical direction, where a non-uniform in z spectral domain decomposition is implemented. This permits more realistic boundary conditions in the vertical and allows shear and stratification profiles to adjust during flow evolution. For each horizontal wavenumber the vertical domain is broken down into 127 subdomains of variable sizes which match their boundary conditions by a mortar method.

The flow is first integrated during several eddy turn over times until it reaches a quasi-stationary state where viscous dissipation balances the external forcing. The external forcing corresponds to a non-uniform mean shear and a density mean profile which are calculated using the meso-scale code MM5. After reaching the quasi-stationary regime, we then perform very long-time integrations to obtain the turbulent fields we will study in this paper.

The code has been parallelized using MPI and the computation has been performed on the parallel machine Nirvana at Los Alamos National Laboratory and the ARL MSRC SGI Origin 3800 machine using a cluster of 32 SGI processors. The spatial resolution is $256 \times 256 \times 512$ and the CPU time to compute one time step is $15s$.

2. Coherent vortex extraction using wavelets

We consider the vorticity field $\vec{\omega} = \nabla \times \vec{v}$ at a given time t, $\vec{v}$ being the velocity field, computed at resolution $N = 2^{3J}$, where N is the number of grid points and J the number of dyadic scales. We use a three-dimensional vector-valued Multi-Resolution Analysis (MRA) of $\left(L^2(R^3)\right)^3$, *i.e.*, a set of nested subspaces $\vec{V}_j \subset \vec{V}_{j+1}$ for $j = 0, ...J-1$, representing the flow at different scales $l = 2^{-j}$. Considering the orthogonal complement spaces $\vec{W}_j = \vec{V}_{j+1} - \vec{V}_j$, we obtain a wavelet representation. Therefore the vorticity vector is developed into an orthogonal wavelet

series,

$$\vec{\omega}(\vec{x}) \;=\; \vec{\bar{\omega}}_{0,0,0}\,\phi_{0,0,0}(\vec{x}) \;+\; \sum_{j=0}^{J-1}\sum_{i_x=0}^{2^j-1}\sum_{i_y=0}^{2^j-1}\sum_{i_z=0}^{2^j-1}\sum_{\mu=1}^{2^n-1} \vec{\tilde{\omega}}^{\mu}_{j,i_x,i_y,i_z}\,\psi^{\mu}_{j,i_x,i_y,i_z}(\vec{x})\,, \tag{1}$$

with $\quad \phi_{j,i_x,i_y i,i_z}(\vec{x}) \;=\; \phi_{j,i_x}(x)\;\phi_{j,i_y}(y)\;\phi_{j,i_z}(z)$, and

$$\psi^{\mu}_{j,i_x,i_y,i_z}(\vec{x}) \;=\; \begin{cases} \psi_{j,i_x}(x)\;\phi_{j,i_y}(y)\;\phi_{j,i_z}(z) & ;\;\mu=1 \quad, \\ \phi_{j,i_x}(x)\;\psi_{j,i_y}(y)\;\phi_{j,i_z}(z) & ;\;\mu=2 \quad, \\ \phi_{j,i_x}(x)\;\phi_{j,i_y}(y)\;\psi_{j,i_z}(z) & ;\;\mu=3 \quad, \\ \psi_{j,i_x}(x)\;\phi_{j,i_y}(y)\;\psi_{j,i_z}(z) & ;\;\mu=4 \quad, \\ \psi_{j,i_x}(x)\;\psi_{j,i_y}(y)\;\phi_{j,i_z}(z) & ;\;\mu=5 \quad, \\ \phi_{j,i_x}(x)\;\psi_{j,i_y}(y)\;\psi_{j,i_z}(z) & ;\;\mu=6 \quad, \\ \psi_{j,i_x}(x)\;\psi_{j,i_y}(y)\;\psi_{j,i_z}(z) & ;\;\mu=7 \quad, \end{cases} \tag{2}$$

where $\phi_{j,i}$ and $\psi_{j,i}$ are the one-dimensional scaling function and the corresponding wavelet, respectively. Due to orthogonality, the scaling coefficients are given by $\vec{\bar{\omega}}_{0,0,0} = \langle \vec{\omega}\,,\,\phi_{0,0,0}\rangle$ and the wavelet coefficients are given by $\vec{\tilde{\omega}}^{\mu}_{j,i_x,i_y,i_z} = \langle \vec{\omega}\,,\,\psi^{\mu}_{j,i_x,i_y,i_z}\rangle$, where $\langle\cdot,\cdot\rangle$ denotes the L^2-inner product.

The extraction algorithm can be summarized as follows:

- given $\vec{\omega}(\vec{x})$, sampled on a grid (x_i, y_j, z_k) for $i,j,k = 0, N-1$, and the total enstrophy $Z = \frac{1}{2}\int |\vec{\omega}|^2 d\vec{x}$,
- perform the three-dimensional wavelet decomposition (*i.e.*, apply the Fast Wavelet Transform to each component of $\vec{\omega}$) to obtain $\vec{\tilde{\omega}}^{\mu}_{j,i_x,i_y,i_z}$ for $j = 0, J-1, i_x, i_y, i_z = 0, 2^{J-1}-1, \mu = 1, ..., 7$,
- compute the threshold $\epsilon_T = (4/3Z\log_e N)^{1/2}$ and threshold the coefficients $\vec{\tilde{\omega}}$ to obtain

$$\vec{\tilde{\omega}}_C \;=\; \begin{cases} \vec{\tilde{\omega}} & \text{for } |\vec{\tilde{\omega}}| > \epsilon_T \\ 0 & \text{for else} \end{cases} \qquad \vec{\tilde{\omega}}_I \;=\; \begin{cases} \vec{\tilde{\omega}} & \text{for } |\vec{\tilde{\omega}}| \le \epsilon_T \\ 0 & \text{for else,} \end{cases} \tag{3}$$

- perform the three-dimensional wavelet reconstruction (*i.e.*, apply the inverse Fast Wavelet Transform) to compute $\vec{\omega}_C$ and $\vec{\omega}_I$ from $\vec{\tilde{\omega}}_C$ and $\vec{\tilde{\omega}}_I$, respectively,
- use Biot-Savart's relation $\vec{V} = (\nabla\times)^{-1}\vec{\omega}$ to reconstruct the coherent and incoherent velocity fields from the coherent and incoherent vorticity fields, respectively.

Note that the decomposition of $\vec{\omega} = \vec{\omega}_C + \vec{\omega}_I$ is orthogonal and hence it follows that $Z = Z_C + Z_C$.

The complexity of the Fast Wavelet Transform (FWT) is of $O(N)$, where N denotes the total number of grid points.

3. Application to the vorticity field

We will first consider the vorticity vector field $\vec{\omega}$ (Fig. 2a) which has been computed at resolution $N = 256\times256\times512$, but for practical reason has been undersampled to $N' = 64^3$. We split the total flow $\vec{V}_T, \vec{\omega}_T$ into coherent $\vec{V}_C, \vec{\omega}_C$ (Fig. 2b) and incoherent flows $\vec{V}_I, \vec{\omega}_I$ (Fig. 2c). We find that only 2.5% of the N' modes are sufficient to represent the coherent flow, which contains 99% of the total energy and 89% of the total enstrophy. We observe that the coherent vorticity field presents the same vortex tubes as those observed in the total vorticity field when we plot the isosurfaces $|\vec{\omega}| = 3/2(Z)^{1/2}$ (Fig. 2a and 2b). In contrast, the incoherent vorticity field (Fig. 2c) does not exhibit any organized structures. If we consider the probability distribution function (PDF) of the vorticity (Fig. 4a), we find the same variability for the coherent vorticity as for the total one (±40), while the variability of the incoherent vorticity is reduced (±10).

As to the PDF of vertical velocity (Fig. 4b), we find very different behaviors: the total and coherent vertical velocities are skewed, varying from -2.3 to 1.5; in contrast the incoherent vertical velocity is not skewed and its behavior is close to Gaussian (Fig. 4b), with a reduced variability (±0.1).If we now plot the energy spectrum (Fig. 4c), we find the same $k^{-5/3}$ scaling for the total and coherent velocity fields up to the wavenumber $k = 20$, with a maximum around $k = 3$ reflecting large scale correlation. For higher wavenumbers, the spectral slope becomes much steeper (about k^{-5}) with the coherent contribution being shifted slightly below the total one. The incoherent field, which contributes no more than 1%, is spread all over the wavenumbers, presenting a $k^{+1/3}$ scaling. This shows some tendency towards decorrelation, although energy equipartition in three dimension corresponds to a k^{+2} scaling. We now propose to investigate other variables, looking for a sharper decorrelation.

4. Application to the potential vorticity field

For this we will consider decomposing the flow into geostrophically balanced components and unbalanced ones. This can be achieved through a Craya basis decomposition (Craya 1958). In the Boussinesq case (for which velocity remains divergent-free), the primitive physical variables, velocity $\vec{V}$ and temperature T, are replaced by three new variables: the quasi-geostrophic (QG) potential vorticity q, the horizontal divergence χ

and the thermal wind imbalance ξ. The first variable corresponds to the flow component in geostrophic balance, while the two other variables characterize the departure from geostrophic and hydrostatic balance. The QG potential vorticity is a scalar field which is transported by the geostrophically balanced horizontal components of the total velocity.

In this paper we will only study the QG potential vorticity field q (Fig. 6a), which has been computed at resolution $N = 256 \times 256 \times 512$ and undersampled to $N'' = 256^3$.

Using the wavelet decomposition as described in Farge, Schneider & Kevlahan 1999, the QG potential vorticity field q is split into coherent q_C and incoherent q_I components which are orthogonal. We find that only 6.8% of the N'' modes are sufficient to represent the coherent QG potential vorticity, which contains 99.6% of the total QG potential enstrophy Z_p. We observe that the coherent QG potential vorticity field presents the same tube-like structures as those observed in the total QG potential vorticity field when we plot the isosurfaces $q = 3/2(Z_p)^{1/2}$ (Fig. 6a and 6b). In contrast, the incoherent QG potential vorticity field (Fig. 6c) does not exhibit any organized structures.

If we consider the probability distribution function (PDF) of the QG potential vorticity (Fig. 5a), we find the same variability for the QG potential coherent vorticity as for the total one (± 100), while the variability of the incoherent vorticity is much reduced (± 4). We find the same spectral behavior for the total and coherent QG potential enstrophy (Fig. 5b) up to wavenumber $k = 100$; the incoherent QG potential enstrophy presents a k^{+2} scaling, characteristic of equipartition between all wavevectors in three dimensions.

We will now check how accurately the nonlinear flow dynamics is preserved by the wavelet filtering. For this we will integrate for 3 eddy turnover times both the total and the coherent potential vorticities and compare the final states. On Fig. 7a and Fig. 7a we check that the two realizations are very similar and exhibit the same structures, both in location and shape.

5. Conclusion

In this paper we have applied the wavelet filtering method to a stably stratified and sheared turbulent flow in three dimensions. Such a flow is highly inhomogeneous since it consists of a central jet subjected to different stratifications above and below the jet core. We have shown that the coherent structures are well extracted by retaining very few wavelet coefficients, which are actually sufficient to predict the flow evolution on few eddy turnover times. We have also shown that the residual flow is

incoherent, presents Gaussian PDFs and a tendency towards decorrelation. This gives us some confidence in being able to statistically model the feedback of the incoherent contributions onto the coherent flow, the evolution of the latter being deterministically computed. In this paper we have also explored the relevance of using the Craya decomposition to gain a better insight into the dynamics of sheared stratified flows. We have first considered the QG potential vorticity which is weakly coupled to the two other Craya variables; the latter correspond to the departure from geostrophic balance. We plan for future work to extend the wavelet filtering to these remaining variables which, in contrast, are strongly coupled together.

Acknowledgments

This work is supported by the AFOSR Contract FG9620-99-1-0300, the DoD HPC Challenge Program, the NSF-CNRS collaboration grant between ASU and CNRS, the French-German program Procope (contract 01220ZE) and the European program TMR (contract FMRX-CT98-0184).

References

Bedard, A.J., Canavero, F. & Einaudi, F. 1986 Atmospheric gravity waves and aircraft turbulence encounters. *J. Atmos. Sci.*, **43**, 2838-2844.

Craya, A. 1958 Contribution à l'analyse de la turbulence associée à des vitesses moyennes. *P.S.T. Minisère de l'Air* (Paris), **345**.

Kaltenbach, H.J., Gerz, T. & Schumann, U. 1994 Large-eddy simulation of homogeneous turbulence and diffusion in stably stratified shear flow, *J. Fluid Mech.* **280**, 1–40.

Tse, K.L., Mahalov, A., Nicolaenko, B. & Fernando, H.J.S. 2001 A spectral domain decomposition method and its application to simulations of shear-stratified turbulence. *Lecture Notes in Physics, Springer-Verlag*, **566**, 353-378.

Farge, M., Schneider, K. & Kevlahan, N. 1999 Non–Gaussianity and Coherent Vortex Simulation for two–dimensional turbulence using an adaptive orthonormal wavelet basis. *Phys. Fluids*, **11**(8), 2187–2201.

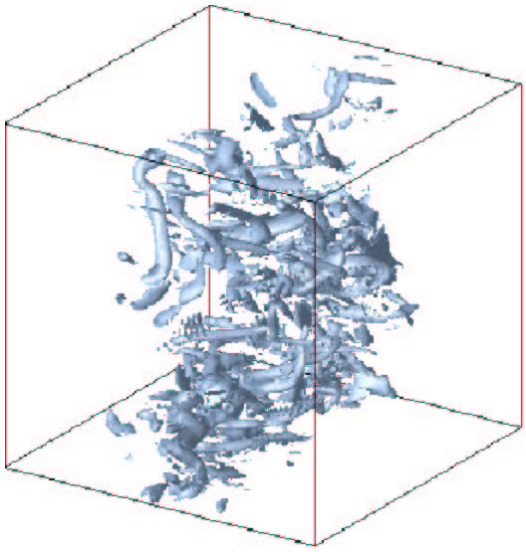

Figure 2a. Modulus of the total vorticity

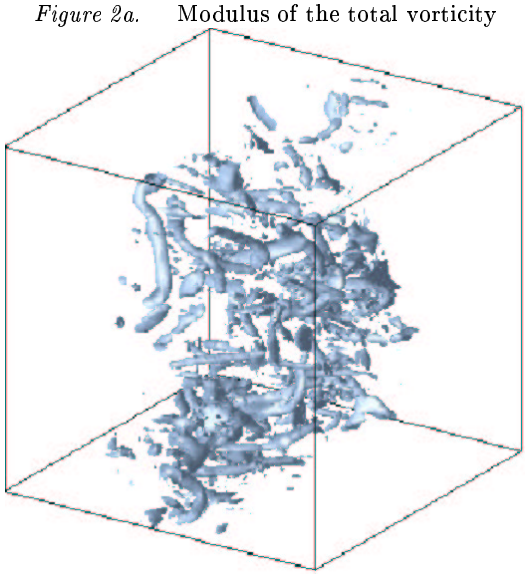

Figure 2b. Modulus of the coherent vorticity

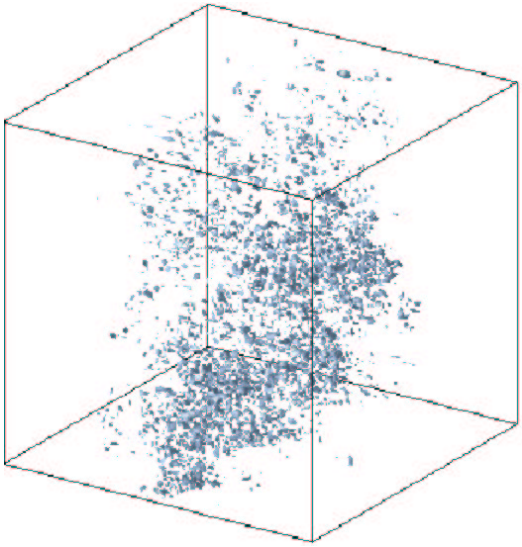

Figure 2c. Modulus of the incoherent vorticity

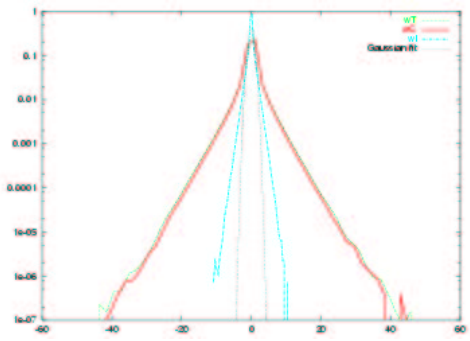

Figure 3a. Vorticity PDF

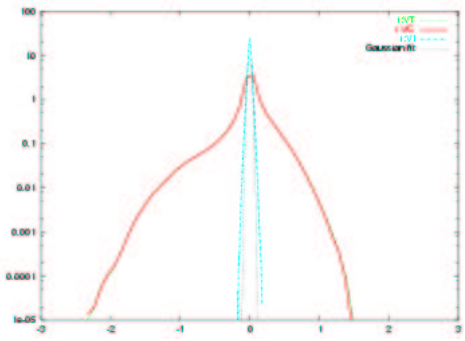

Figure 3b. Vertical velocity PDF

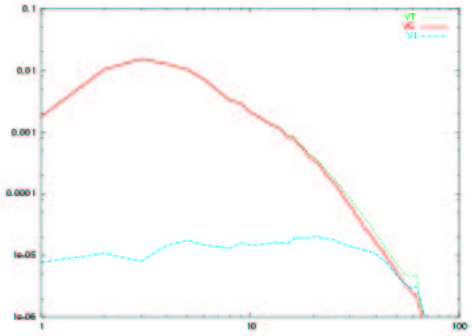

Figure 3c. Energy spectrum

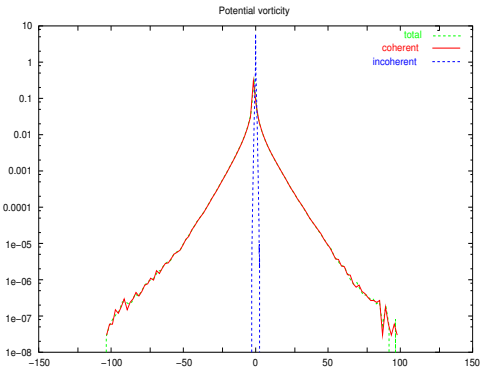

Figure 4a. Potential vorticity PDF

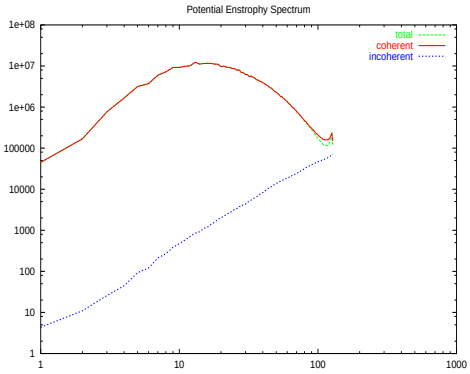

Figure 4b. Potential enstrophy spectrum

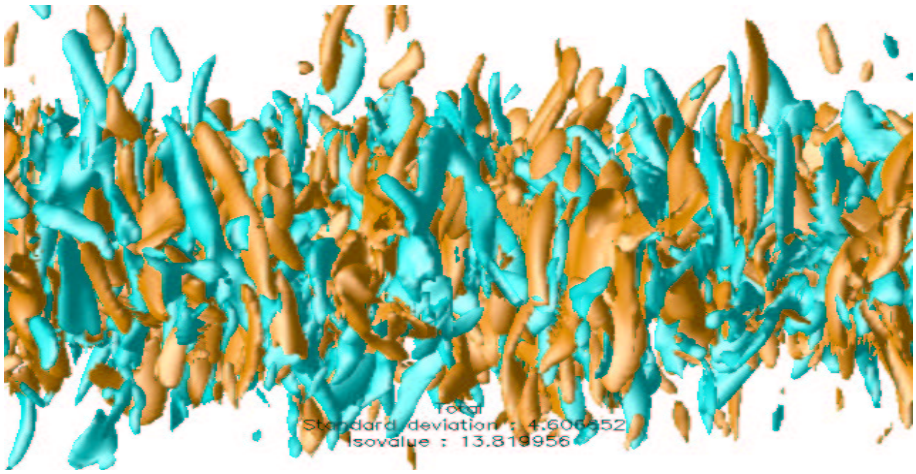

Figure 5a. Total potential vorticity

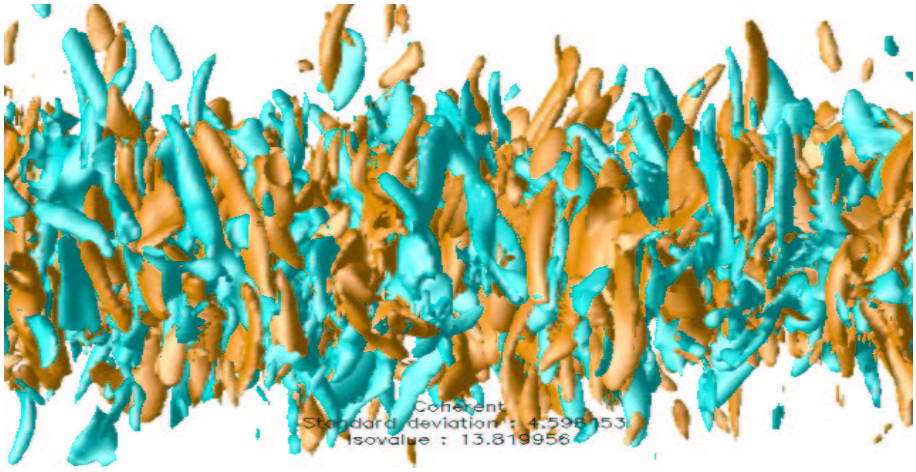

Figure 5b. Coherent potential vorticity

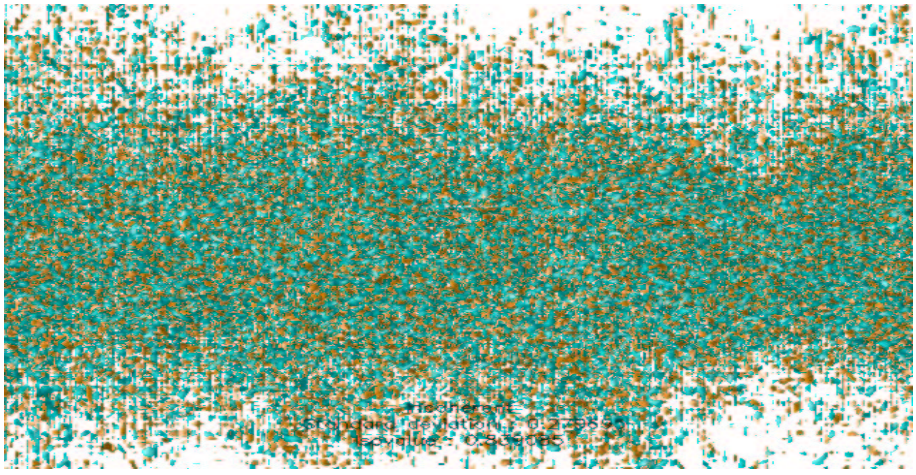

Figure 5c. Incoherent potential vorticity

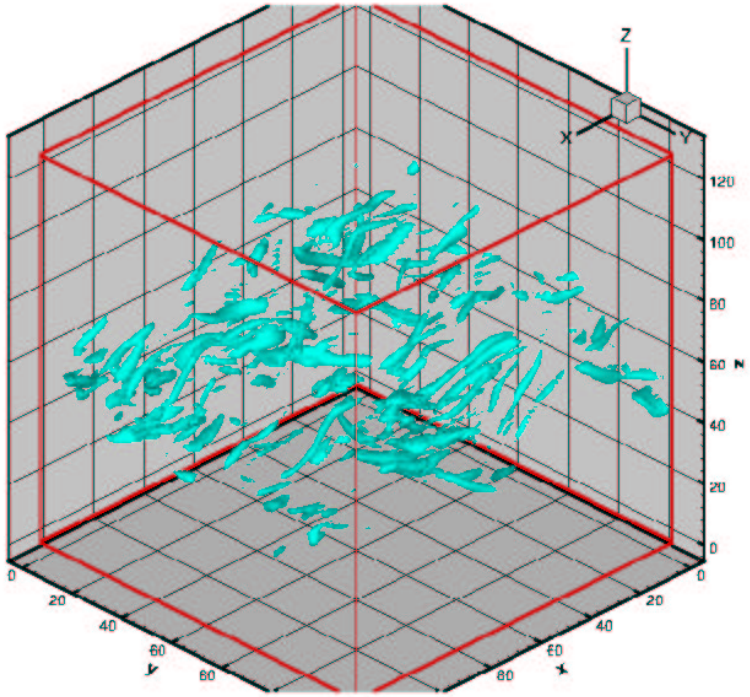

Figure 6a. Total potential vorticity after integration

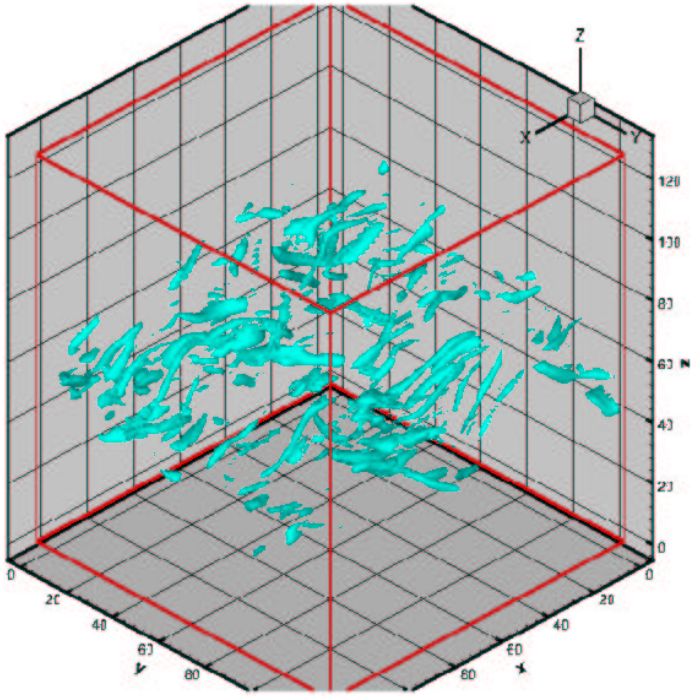

Figure 6b. Coherent potential vorticity after integration